Engineering d-p Orbital Hybridization with P, S Co-Coordination Asymmetric Configuration of Single Atoms Toward High-Rate and Long-Cycling Lithium–Sulfur Battery

Chenxu Dong, Changning Ma, Cheng Zhou, Yongkun Yu, Jiajing Wang, Kesong Yu, Chunli Shen, Jiapei Gu, Kaijian Yan, Aqian Zheng, Minjian Gong, Xu Xu, and Liqiang Mai**

Single-atom catalysts (SACs) have been increasingly explored in lithium–sulfur (Li–S) batteries to address the issues of severe polysulfide shuttle effects and sluggish redox kinetics. However, the structure-activity relationship between single-atom coordination structures and the performance of Li–S batteries remain unclear. In this study, a P, S co-coordination asymmetric configuration of single atoms is designed to enhance the catalytic activity of Co central atoms and promote d-p orbital hybridization between Co and S atoms, thereby limiting polysulfides and accelerating the bidirectional redox process of sulfur. The well-designed SACs enable Li–S batteries to demonstrate an ultralow capacity fading rate of 0.027% per cycle after 2000 cycles at a high rate of 5 C. Furthermore, they display excellent rate performance with a capacity of 619 mAh g^{-1} at an ultrahigh rate of 10 C due to the efficient catalysis of CoSA-N$_3$PS. Importantly, the assembled pouch cell still retains a high discharge capacity of 660 mAh g^{-1} after 100 cycles at 0.2 C and provides a high areal capacity of 4.4 mAh cm^{-2} even with a high sulfur loading of 6 mg cm^{-2}. This work demonstrates that regulating the coordination environment of SACs is of great significance for achieving state-of-the-art Li–S batteries.

1. Introduction

The development of lithium–sulfur (Li–S) batteries has garnered increasing attention as the next-generation energy storage system due to their high theoretical specific capacity (1675 mAh g^{-1}) and gravimetric energy density (2600 Wh kg^{-1}), alongside the abundance, low cost (<\$150 ton^{-1}), and eco-friendliness of sulfur.[1–4] However, the commercialization of the Li–S batteries is significantly hindered by the substantial volume expansion (≈80%), sluggish sulfur oxidation/reduction kinetics, and severe shuttle effect, resulting in poor practical capacity, cycle stability, and rate performance.[5–7] To address these challenges, numerous studies have explored active materials to function as sulfur hosts, confining and catalyzing soluble polysulfides.[8–10] Initially, a variety of carbon-based materials were employed to accommodate volume expansion and adsorb polysulfides. However, their weak physical adsorption makes it challenging to mitigate the shuttle effect.[11,12] Moreover, these carbon materials lack sufficient active sites to effectively enhance the conversion of polysulfides, leading to sluggish polysulfide redox kinetics. Additionally, to mitigate the complex shuttle effect and enhance redox kinetics, polar materials such as metal nanoparticles, defective materials, and metal compounds with strong electrocatalytic properties were employed to accelerate polysulfide redox kinetics.[2,13–16] Nevertheless, achieving satisfactory catalytic performance requires a substantial quantity of catalysts, potentially significantly diminishing the overall energy density of the Li–S battery.

Single-atom catalysts (SACs) have emerged as promising candidates and are increasingly studied in the context of the Li–S batteries owing to their distinctive electronic structure, maximal atom utilization, and high catalytic activity with minimal mass loading.[17–19] SACs exhibit the ability to establish robust polar-polar interactions with polysulfides, effectively restraining the migration of soluble polysulfides and expediting the successive conversion of polysulfides.[8,20,21] Presently, extensive research on SACs in the Li–S batteries predominantly centers on d-region transition metals, specifically coordinated in the form of M-N$_4$ (Fe, Co, Ni, Zn, etc.).[22–25] Recent investigations emphasize the correlation between the catalytic activity/selectivity of SACs for electrochemical reactions in the Li–S batteries and the central metal atom along with its coordination environment.[26–28] However, in the case of non-polar M-N$_4$ coordination, symmetric electron distribution limits the activity of the central metal atom due to the high electronegativity of N atoms, adversely

---

C. Dong, C. Ma, C. Zhou, Y. Yu, J. Wang, K. Yu, C. Shen, J. Gu, K. Yan, A. Zheng, M. Gong, X. Xu, L. Mai
State Key Laboratory of Advanced Technology for Materials Synthesis and Processing
International School of Materials Science and Engineering
Wuhan University of Technology
Wuhan, Hubei 430070, P. R. China
E-mail: xuxu@whut.edu.cn; mlq518@whut.edu.cn

The ORCID identification number(s) for the author(s) of this article can be found under https://doi.org/10.1002/adma.202407070

DOI: 10.1002/adma.202407070

affecting the redox kinetics of polysulfides.[29–32] Consequently, altering the number of coordinated nitrogen atoms around the central metal atom to achieve asymmetric electron arrangement proves to be an effective strategy, which can effectively enhance the adsorption of sulfur by the active center and the bidirectional redox kinetics of polysulfides.[33,34] Additionally, the introduction of heteroatoms with varying electronegativity (such as S, P, O, B, etc.) into the first shell layer offers an effective mean to regulate the 3d orbital electronic structure of central metal atoms, which could adjust the charge density difference to strengthen the catalytic performance of SACs.[35–37] Exemplifying these strategies, Chen and colleagues designed an oversaturated Fe-N_5 coordination structure (Fe-N_5-C) as a sulfur host material, effectively mitigating the shuttle effect and enhancing the redox conversion of polysulfides.[38] In another instance, Sun et al. prepared a novel single-atomic iron mediator with a designed FeN_3P_1 coordination structure to enhance the bidirectional conversion of polysulfides, yielding satisfactory electrochemical performance.[39] While these strategies have indeed proven effective in enhancing the activity of single-atom centers and improving the performance of Li–S batteries, achieving precise control over the coordination environment of single-atom catalysts, especially through the use of multiple heteroatoms to regulate their electronic structures, remains a substantial challenge. The structure-activity relationship between single-atom coordination structure and the performance of Li–S batteries remains unclear.[26] Therefore, an urgent need exists for the atomic-level regulation of the coordination environment of single-atom catalysts and a comprehensive elucidation of the mechanism behind how changes in the electronic structure of single-atom catalysts enhance the redox kinetics of polysulfides, a subject that has been scarcely reported.

Herein, the present study developed a unique sulfur host by designing a P, S co-coordination asymmetric configuration of single atoms within a N-doped carbon regular dodecahedral nanocage (CoSA-N_3PS). This configuration aims to confine polysulfides and enhance the redox kinetics of polysulfides through a two-step pyrolysis method. The precise coordination of the Co single-atom active center with N, P, and S atoms has been clearly demonstrated using various microscopic and spectroscopic methods and study the effect of pyrolysis temperature on the formation of different coordination structures to achieve precise control of the coordination environment of SACs. Additionally, theoretical calculations support the assertion that the CoSA-N_3PS configuration not only enhances the adsorptive activity of the Co-active centers for capturing polysulfides but also accelerates the bidirectional conversion between polysulfides and Li_2S/Li_2S_2 due to the d-p orbital hybridization between single Co atoms and S atoms. As a result of this design, batteries with S@CoSA-N_3PS cathodes exhibit highly satisfactory electrochemical performance. Notably, these batteries demonstrate remarkable cycle stability, featuring a capacity fading rate of only 0.037% per cycle after 1000 cycles at 1 C, and retaining 86.4% capacity after 200 cycles at 0.5 C. Moreover, the batteries exhibit satisfactory rate performance, delivering a capacity of 619 mAh g^{-1} at a high discharge rate of 10 C.

2. Results and Discussion

The preparation procedure and catalytic reaction mechanism of the S@CoSA-N_3PS cathode through the two-step pyrolysis method are elucidated in **Figure** 1a. Initially, the in-situ polymerization of poly(cyclotriphospazeneco-4,4′-sulfonyldiphenol) (PZS) results in the encapsulation of ZIF-8 particles, forming a ZIF-8@PZS core-shell structure as a pyrolysis precursor. Subsequently, the carbonization of ZIF-8@PZS in an inert atmosphere triggers the diffusion of P and S species from the PZS shell with Zn^{2+} from the internal ZIF-8 nanoparticles, following a Kirkendall effect. Owing to the smaller radius of Zn^{2+}, their outward diffusion rate exceeds that of the P and S species, leading to the creation of a hollow shell structure co-doped with N, P, and S (NPS). Simultaneously, the low boiling point of Zn induces the formation of numerous vacancies through evaporation during the pyrolysis process. Subsequent to this, the precursor cobalt is adsorbed onto the evaporated sites of Zn and P, S heteroatoms replace one N atom to form the first shell coordination after further 950 °C pyrolysis, ultimately resulting in the highly coordinated CoSA-N_3PS catalyst. To further prove the mechanism of forming the exact CoSA-N_3PS configuration, DFT calculation of different configurations was conducted (Figure S1, Supporting Information). By comparing the energies of different systems with four coordination or five coordination, it can be found that in P, S co-doped systems, a Co atom tends to coordinate more with three N atoms, one S atom, and one P atom, thus forming the most stable structure rather than the four-coordination structure such as CoSA-N_2P_2 or CoSA-NP_2S etc (Figure S2, Supporting Information). Therefore, in a system where P and S heteroatoms coexist, CoSA-N_3PS catalyst will ultimately be generated as the final product theoretically according to the laws of thermodynamics. The structural and morphological characterizations of CoSA-N_3PS and intermediate products were conducted using SEM and TEM. As depicted in Figure S3a,b (Supporting Information), CoSA-N_3PS exhibits a regular dodecahedral morphology of ≈150 nm, similar to ZIF-8 (Figure S4a,b, Supporting Information), ZIF-8@PZS (Figure S5a,b, Supporting Information), and NPS (Figure S6a,b, Supporting Information). This observation indicates that CoSA-N_3PS maintains a consistent morphology after the two pyrolysis processes. Furthermore, S@CoSA-N_3PS still retains its original appearance with no bulk sulfur observed, suggesting that sulfur is evenly distributed on both the surface and inside (Figure S7a,b, Supporting Information). As depicted in Figure 1c, the edges and corners of ZIF-8@PZS appear slightly blurred compared to ZIF-8 nanoparticles (Figure 1b), revealing a characteristic core-shell structure and indicating the complete coating of ZIF-8 by PZS. In Figure 1d, the CoSA-N_3PS displays a well-defined regular dodecahedral hollow structure similar to NPS (Figure 1c), suggesting that the introduction of a single Co atom does not compromise the hollow structure. These findings affirm the successful synthesis of CoSA-N_3PS hollow dodecahedral nanocages with uniform morphology distribution, facilitating sulfur loading and restricting polysulfides to the cathode during the electrochemical process. Additionally, aberration-corrected high-angle annular dark-field scanning TEM (AC-HAADF-STEM) was conducted to prove the existence

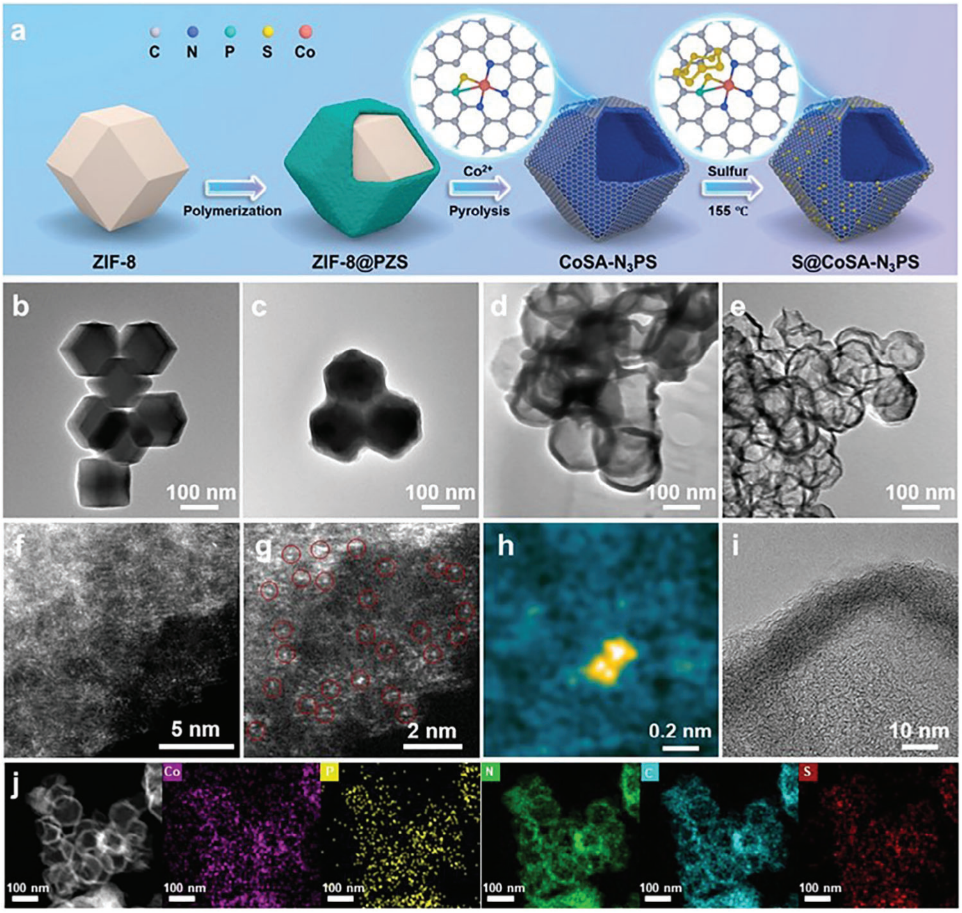

Figure 1. a) The preparation procedure and catalytic mechanism of S@CoSA-N_3PS. b–e) the TEM images of (b) ZIF-8, (c) ZIF-8@PZS, (d) NPS and (e) CoSA-N_3PS nanocages. f) Atomic-resolution HAADF-STEM image. g,h) Enlarged intensity image of Co single atoms in CoSA-N_3PS. i) HRTEM image. j) STEM image, and corresponding elemental mapping images of CoSA-N_3PS.

of Co single atoms. Isolated bright dots observed in Figure 1f–h signify the uniform dispersion of Co single atoms on a carbon substrate. The atomic ratios of Co, N, P, and S elements are 0.1%, 8.2%, 1.32%, and 2.00%, respectively, according to the EDS mapping (Table S1 and Figure S8, Supporting Information). The crystallographic structures of CoSA-N_3PS were analyzed by XRD patterns (Figure S9a, Supporting Information), revealing two broad diffraction peaks at ≈25° and 45° corresponding to the (002) and (101) faces of graphitic carbon. This is consistent with the pattern of NPS, suggesting the absence of Co nanoparticles during the pyrolysis process. The XRD patterns of ZIF-8 and ZIF@PZS further validate the successful synthesis of intermediate products (Figure S9b, Supporting Information). The HRTEM image illustrates poor crystallization of CoSA-N_3PS, aligning with the XRD results (Figure 1i). Moreover, the HADDF-STEM image and its corresponding energy-dispersive spectroscopy (EDS) mappings of CoSA-N_3PS reveal the homogeneous distribution of Co, N, P, and S atoms on the carbon substrate (Figure 1j). Furthermore, EDS mapping after sulfur loading demonstrates the uniform distribution of N, P, S, and Co atoms, confirming that sulfur adheres uniformly to the interior and surface of CoSA-N_3PS nanocages (Figure S10, Supporting Information). Additionally, there are two peaks around 1337 and 1590 cm^{-1} of CoSA-N_3PS, representing the D band and G band of sp2-hybridized carbon atoms. The ratio of the two bands of CoSA-N_3PS is ≈1.03, closely resembling CoN_4 (1.01) and NPS (1.02), indicating a similar degree of graphitization (Figure S11, Supporting Information). The Brunauer–Emmett–Teller (BET) analysis reveals a high surface area of 756.9 m^2 g^{-1} for CoSA-N_3PS with the BJH desorption average pore diameter of 3.9 nm, which is advantageous for high sulfur loading and polysulfide confinement (Figure S12, Supporting Information). Additionally, thermogravimetric analysis demonstrates a high sulfur content of 77% (Figure S13, Supporting Information). Moreover, the atomic ratios of Co, N, P, and S elements are also tested by Inductively coupled plasma optical emission spectrometry (ICP-OES) and Elemental Analyzer (EA) (Table S2, Supporting Information).

The X-ray photoelectron spectra (XPS analysis was employed to investigate the chemical state and coordination environment of CoSA-N_3PS, revealing the co-existence of Co, C, N, P, and S elements. The high-resolution C 1s spectrum exhibits four peaks at 284.8, 291.7, 289.1, and 285.8 eV, corresponding to C═C, C—N, C—P, and C—S, respectively (Figure S14, Supporting Information). The N 1s spectrum is deconvoluted into five peaks assigned to pyridinic N (398.4 eV), pyrrolic N (400.9 eV), graphitic N (402.7 eV), oxidized N (403.9 eV), and Co-N bond (399.9 eV)

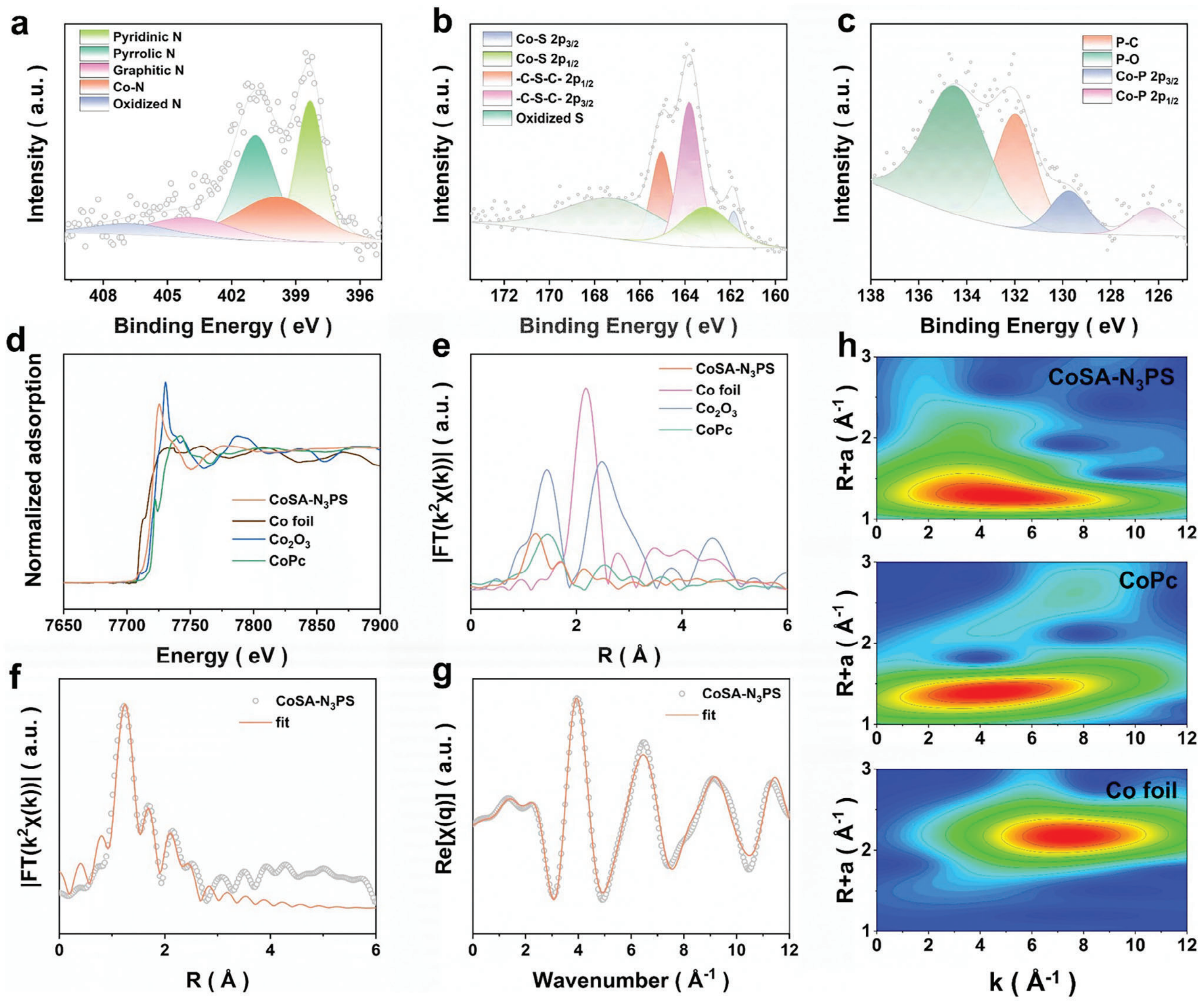

Figure 2. a) N 1s, b) S 2p, c) P 2p XPS spectra of CoSA-N_3PS. d) Co K-edge X-ray absorption near edge structure (XANES) spectra of CoSA-N_3PS, Co_2O_3, CoPc, and Co foil. e) FT-EXAFS at the Co K-edge. f) FT-EXAFS fitting curves in the R space of CoSA-N_3PS (g) XANES spectra in q space and fitting curves of CoSA-N_3PS. h) Co K-edge WT-EXAFS contour plots of different samples.

(**Figure 2a**). In the P spectrum, four peaks at 131.9, 134.5, 129.7, and 126.2 eV are observed, which are ascribed to P—C, P—O, and the $2p_{3/2}$, $2p_{1/2}$ splitting of Co—P (Figure 2b). The S spectrum (Figure 2c) displays five peaks at 162.9, 161.8, 165.0, 163.8, and 167.2 eV, which corresponds to the $2p_{1/2}$, $2p_{3/2}$ of splitting Co—S, $2p_{1/2}$, $2p_{3/2}$ of splitting C—S—C, and oxidized S. In addition, the atomic ratios of Co, N, P, and S elements are 0.29%, 8.48%, 1.14%, and 1.41% which are measured by XPS analysis, respectively (Figure S15, Supporting Information). These results affirm that the Co single atom coordinates with N, P, and S atoms, indicating that the presence of P and S atoms alters the coordination environment of Co single atoms. Moreover, the local structure and coordination environment of CoSA-N_3PS were probed using synchrotron-radiation-based X-ray absorption near-edge structure (XANES) spectra and Fourier-transformed extended X-ray absorption fine structure (FT-EXAFS) characterization. The Co K-edge XANES spectroscopy, analyzed alongside Co foil, Co_2O_3, and CoPC (Figure 2d), suggests that the valence state of Co falls between 0 and +3. The FT-EXAFS spectra of CoSA-N_3PS display two main peaks at 1.32 and 1.78 Å in R space, corresponding to the Bond distance between Co and light atoms (N, P, S, etc.). The peak at ≈2.2 Å representing the Co—Co bond is not clearly observed in CoSA-N_3PS, confirming the atomic dispersion of Co atoms (Figure 2e). To delve deeper into the coordination information of CoSA-N_3PS, the test curves were fit analyzed (Figure 2f,g; Figure S16, Supporting Information). The fitting curve reveals a main peak at 1.32 Å and a sub-strong peak at 1.80 Å, attributed to Co—N, Co—P, and Co—S bond coordination. The structure parameters extracted from the fitting propose a plausible coordination structure of CoSA-N_3PS (Table S3, Supporting Information). Additionally, to demonstrate the atomic coordination structure of Co atoms, wavelet transform (WT) analysis was conducted, offering clear resolution in both R and k spaces. The WT-transform contour plots of CoSA-N_3PS exhibit the strongest intensity at ≈4.2 Å, close to CoPc, which is derived from the scattering between Co atoms and light atoms. In comparison, the WT-transform contour plots of Co foil show a maximum intensity at 7.4 Å, attributed to the Co—Co contribution, further affirming the atomic distribution of Co single atoms (Figure 2h). To further investigate the formation mechanism of P, S heteroatoms coordinated single atom and the universality of preparing heteroatom coordinated single-atom catalysts, a series of cobalt single atom catalysts were prepared by pyrolysis at 1050 and 1150 °C. As the pyrolysis temperature increases, the EXAFS spectra exhibit a higher intensity at 1.93 and 1.90 Å, which is ascribed to the Co-S/P scattering, proving that P or S atoms replaced nitrogen atoms (Figures S17 and S18, Supporting Information). Further extraction of coordination number information for N, P, and S atoms reveals that the most likely coordination configuration at 1050 °C pyrolysis temperature is CoSA-N_2PS_2, while the most likely coordination configuration at 1150 °C pyrolysis temperature is CoSA-NPS_3 (Table S3, Supporting Information). These results demonstrate that as the pyrolysis temperature increases, P and S heteroatoms will replace more N atoms coordinated by Co single atom to form a P and S co-coordinated structure, thereby proving that pyrolysis temperature can effectively regulate the coordination environment of single atoms. Furthermore, the high-resolution XPS spectra at the N region of CoSA-N_3PS, CoSA-N_2PS_2, and CoSA-NPS_3 show that the content of pyridine-N and Co—N decreases with the increase of pyrolysis temperature, which proves that S/P heteroatoms replace N atoms with the increase of pyrolysis temperature (Figure S19, Supporting Information). In addition, the XRD patterns of CoSA-N_2PS_2 and CoSA-NPS_3 both show two broad diffraction peaks which are similar with CoSA-N_3PS, corresponding to the (002) and (101) faces of graphitic carbon (Figure S20, Supporting Information). The TEM images of CoSA-N_2PS_2 and CoSA-NPS_3 show a similar hollow morphology with CoSA-N_3PS, manifesting that increasing the temperature will not affect the morphology of the catalysts obviously (Figures S21 and S23, Supporting Information). Additionally, the HAADF-STEM images and corresponding EDS mapping prove the uniform distribution of Co, N, S, P in CoSA-N_2PS_2 and CoSA-NPS_3 (Figures S22 and S24, Supporting Information). Therefore, these results indicate that adjusting the pyrolysis temperature can effectively regulate the atomic coordination structure of the catalyst and demonstrate that the formation mechanism of CoSA-N_3PS structure during pyrolysis at 950 °C is P, and S heteroatoms replace one N atom to form the most stable structure.

To investigate the impact of the asymmetric configuration of CoSA-N_3PS on catalytic performance, symmetrical cells utilizing different cathodes in a Li_2S_6 electrolyte were subjected to cyclic voltammetry (CV) measurements (**Figure** 3a). Two distinct redox peaks were observed at a scan rate of 5 mV s^{-1}, corresponding to the conversion between S_8, Li_2S_6, and Li_2S. Notably, CoSA-N_3PS exhibited a higher response current compared to CoSA-N_4 and NPS samples, indicating faster redox kinetics of polysulfides. Additionally, the initial three cycles of the symmetrical cells with CoSA-N_3PS demonstrated good reversibility during the polysulfides conversion process (Figure 3b). Moreover, at a scan rate of 50 mV s^{-1}, the two redox peaks disappeared due to the rapid scan speed, yet CoSA-N_3PS still exhibited more satisfactory catalytic performance (Figure 3c). The adsorptive performance of the cathode material for polysulfides plays a crucial role in mitigating the shuttle effect. Therefore, a visualized adsorption test and UV–vis spectroscopy analysis were performed with a 2 mᴍ Li_2S_6 solution (Figure 3d). After standing for 12 h, the Li_2S_6 solution in the CoSA-N_3PS bottle turned colorless and transparent, while the solutions of the other three systems retained a light yellow or yellow color. These results demonstrate that the P, S co-coordination enhances the adsorptive activity of Co single atoms for polysulfides, beneficial for suppressing the shuttle effect. Furthermore, X-ray photoelectron spectroscopy (XPS) analysis was performed to further elucidate the adsorption mechanism of CoSA-N_3PS. In the Li 1s spectrum, two peaks at 55.8 and 56.7 eV represented the Li—S bond and Li—N bond, indicating abundant N sites preferentially interact with Li in Li_2S_6 (Figure S25a, Supporting Information). The S spectrum was deconvoluted into four species after CoSA-N_3PS adsorption of Li_2S_6 at 162.3/163.8, 164.5/165.2, 167.4/169.3, and 169.4/170.6 eV, corresponding to terminal sulfur (ST^{-1}), bridged sulfur (SB^0), thiosulfate, and polythionate species (Figure S25b, Supporting Information). As a comparison, the S spectrum of NPS after Li_2S_6 adsorption suggested that terminal sulfur almost disappears, likely due to the absence of Co single atoms (Figure S26, Supporting Information).

To delve deeper into the impact of CoSA-N_3PS catalysis on the oxidation and reduction processes of Li_2S, various electrocatalytic tests were conducted. Three-electrode linear-sweep voltammetry revealed that CoSA-N_3PS exhibited the highest current response and the smallest Tafel slope (186 mV dec^{-1}) during Li_2S oxidation compared to the other samples, indicating that the P, S co-coordination with Co single atoms is advantageous for Li_2S decomposition (Figure 3e). These findings are consistently supported by the denucleation test shown in Figure S27a–c (Supporting Information). The CoSA-N_3PS/Li_2S_8 cathode displayed a higher capacity (1042 mAh g^{-1}) compared to CoSA-N_4 (850 mAh g^{-1}) and NPS (834 mAh g^{-1}). Furthermore, As depicted in Figure 3g-i, Li_2S nucleation testing with different cathode composites in Li_2S_8 electrolyte demonstrated that CoSA-N_3PS composites exhibited the highest response current and earlier response current peaks (5276 s) compared to CoSA-N_4 (5332 s) and NPS (5361 s), indicating a faster Li_2S nucleation process on the CoSA-N_3PS composite. Additionally, the calculated nucleation capacity of CoSA-N_3PS reached as high as 1018 mAh g^{-1}, surpassing CoSA-N_4 (446 mAh g^{-1}) and NPS (147 mAh g^{-1}), suggesting that the CoSA-N_3PS catalyst enhances the liquid–solid reaction of polysulfides. These results affirm that the asymmetric coordination of P and S regulates the d-orbitals of Co single atom centers, leading to excellent catalytic performance and enhanced bidirectional redox kinetics in the conversion of polysulfides.

To comprehensively assess the impact of the asymmetric high-coordination CoSA-N_3PS catalyst on Li–S cell performance, Li–S batteries were assembled with different cathodes (S@CoSA-N_3PS, S@CoSA-N_4, and S@NPS) and a lithium anode. First, the cyclic voltammetry (CV) curves with a charge and discharge voltage window of 1.7–2.8 V at a scan rate of 0.1 mV s^{-1} are presented in **Figure** 4a. Two reduction peaks are observed at ≈2.2–2.4 and 1.9–2.1 V, corresponding to multistep reduction from S_8 to soluble Li_2S_n ($4 \le n \le 8$) and then to insoluble Li_2S or Li_2S_2 during the discharge process. One oxidation peak at ≈2.3–2.4 V

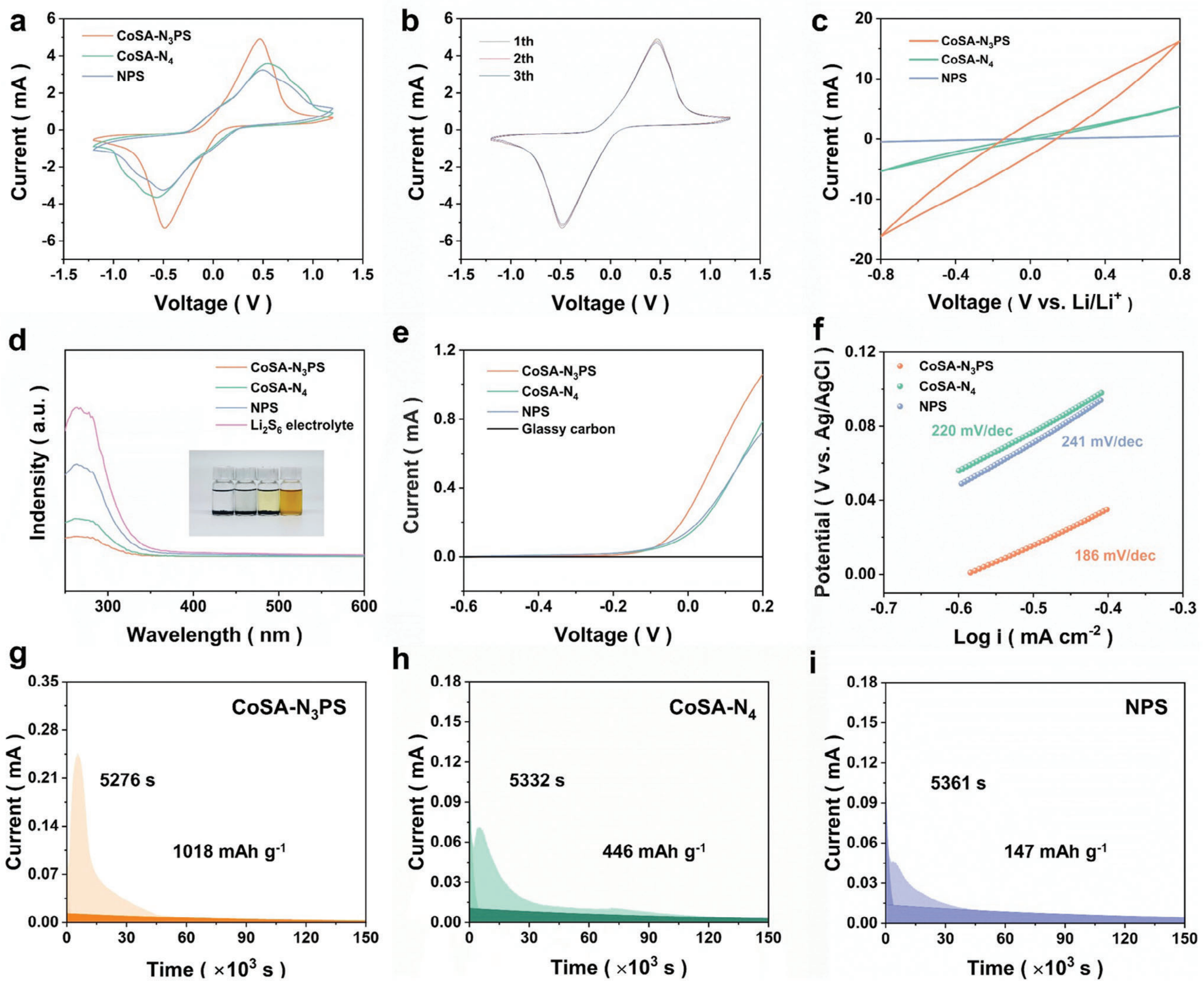

Figure 3. a,b) Cyclic voltammetry (CV) curves and initial three cycles of CV curves of symmetric batteries at a scan of 5 mV s^{-1}. c) CV curves of symmetric batteries at a scan of 50 mV s^{-1}. d) UV–vis absorption spectra in 2 mmol L^{-1} Li_2S_6 solution. Inset: digital photo of adsorption tests of: (1) bare Li_2S_6, (2) NPS/Li_2S_6, (3) CoSA-N_4/Li_2S_6, and (4) CoSA-N_3PS/Li_2S_6, respectively. e,f) Linear sweep voltammetry curves and derived Tafel plots of different composites. Potentiostatic discharge curves of Li_2S nucleation with CoSA-N_3PS (g), CoSA-N_4 (h), and NPS (i).

corresponds to the dissolution of Li_2S or Li_2S_2 to Li_2S_n ($4 \le n \le 8$) and finally to S_8 during the charge process. The CV curve of the S@CoSA-N_3PS cathode displays two reduction peaks at 2.3 and 2.04 V and two oxidation peaks at 2.34 and 2.39 V, which are close to the standard redox potential of the Li–S batteries and exhibit a potential polarization as low as 0.04 V. In comparison, the CV curves of S@CoSA-N_4 and S@NPS show larger potential polarization and response current than that of S@CoSA-N_3PS, demonstrating that CoSA-N_3PS can effectively enhance the redox reaction of polysulfides. Additionally, the initial three cycles of CV curves of CoSA-N_3PS exhibit good repeatability, demonstrating CoSA-N_3PS possesses good electrochemical reversibility and catalytic persistence during the charge–discharge cycles (Figure S28, Supporting Information). Moreover, Tafel curves calculated from CV curves are also shown in Figure S29a,b, (Supporting Information) to demonstrate the effect of different catalysts on the redox reaction. The Tafel slope for reduction and oxidation peaks of S@CoSA-N_3PS cathode are significantly smaller than CoSA-N_4 and NPS cathode, certifying the fast redox kinetics of CoSA-N_3PS for polysulfides conversion. These results suggest that the structure of P, S co-coordination is able to improve the activity of the Co single atom center, thereby enhancing the bidirectional redox reaction and reducing potential polarization for the Li–S batteries. Additionally, the multiscan CV curves from 0.1–0.5 mV s^{-1} of CoSA-N_3PS, CoSA-N_4, and NPS are shown in Figure S30a–c (Supporting Information). Li-ion diffusion ability can be evaluated from the Randles-Sevcik equation: $Ip = (2.69 \times 10^5) \times n^{1.5} \times A \times DLi^{+0.5} \times C\_Li^+ \times v^{0.5}$. The calculated slope of CoSA-N_3PS is higher than other systems, proving that CoSA-N3PS possesses faster Li-ion diffusion capacity and redox conversion (Figure S31a–c, Supporting Information). Moreover, the galvanostatic charge/discharge curves of the batteries

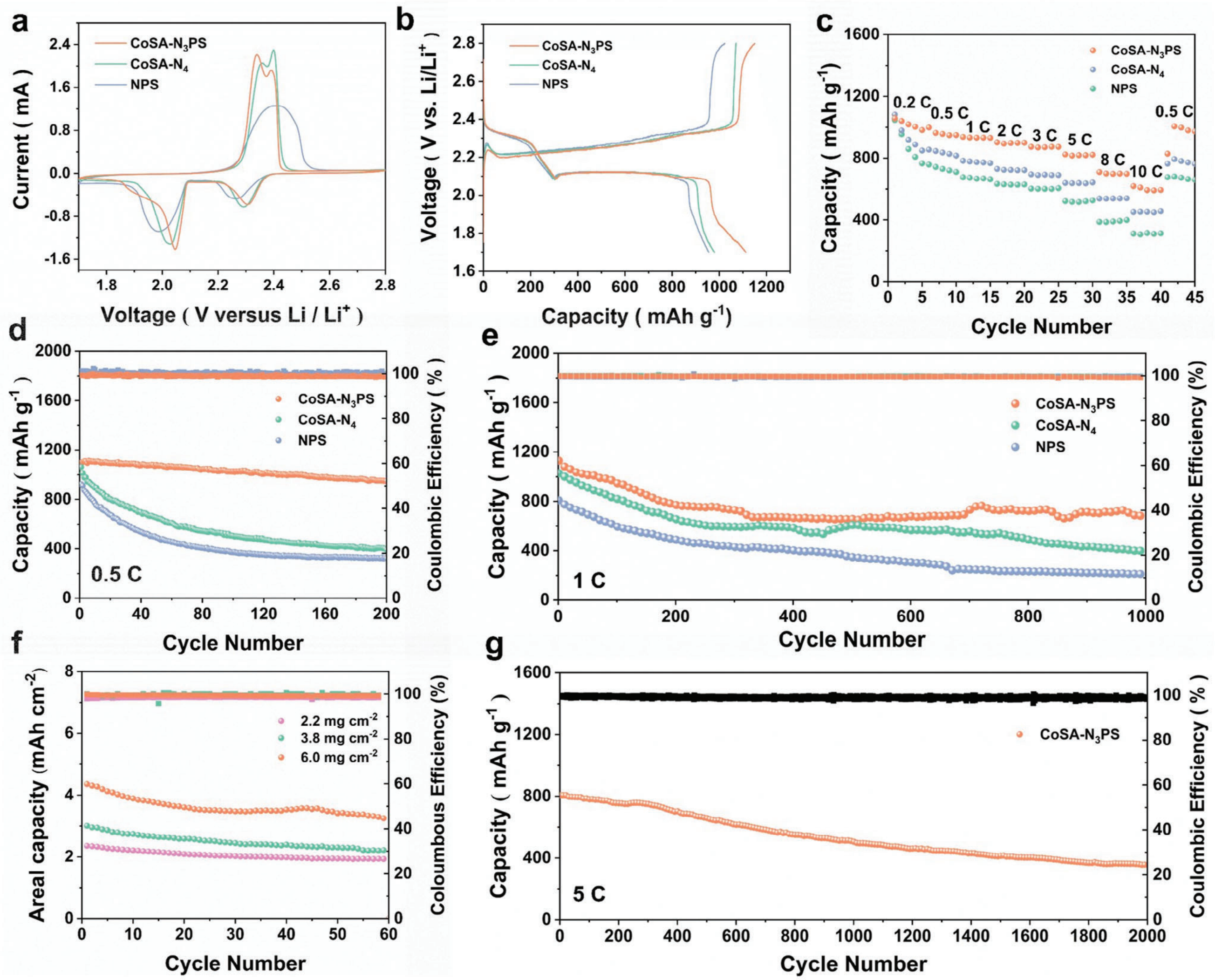

Figure 4. a) CV curves of S@CoSA-N_3PS, S@CoSA-N_4, and S@NPS cathodes at 0.1 mV s^{-1}. b) Galvanostatic charge–discharge curves at the current density of 0.2 C. c) Rate performances of S@CoSA-N_3PS, S@CoSA-N_4, and S@NPS cathodes. d) Cycling performances at 0.5 C. e) Long-term cycling performances at 1 C. f) Cycling performances of S@CoSA-N_3PS cathodes with various sulfur loadings. g) Long-term cycling performances of S@CoSA-N_3PS electrode at 5 C.

with S@CoSA-N_3PS, S@CoSA-N_4, and S@NPS cathodes-based cells at 0.2 C were represented in Figure 4b. The curve displays one charge plateau and two discharge plateaus, which are in accordance with the reaction mechanism of the Li–S batteries. The potential polarization between the charge plateau and the second discharge plateau of CoSA-N_3PS (139 mV) is smaller than CoSA-N_4 (141 mV) and NPS (149 mV), indicating the faster polysulfides conversion with S@CoSA-N_3PS cathode. Another quantitative evaluation of catalytic activity for polysulfides conversion is the value of Q2/Q1, from which Q1 represents the capacity of the first discharge plateau, ascribing to the reaction from S_8 to Li_2S_4 and Q2 represents the capacity of the second discharge plateau, corresponding to the liquid–solid conversion. The value of Q2/Q1 of the batteries with CoSA-N_3PS cathode (2.65) is larger than that with CoSA-N_4 (2.27) and NPS (2.25) cathodes, indicating higher catalytic activity leading to more complete reactions for the conversion from soluble Li_2S_n to solid Li_2S/Li_2S_2 (Figure S32, Supporting Information). Moreover, the S@CoSA-N_3PS cathode exhibits a lower voltage step and smaller voltage dip than the other two examples, manifesting a lower overpotential during the redox conversion of polysulfides (Figure S33a,b, Supporting Information).

To comprehensively investigate the impact of coordination control of single-atom catalysts on the rate and cycling performance of the Li–S batteries, the rate performance was evaluated at a current density of 0.2 C, 0.5 C, 1 C, 2 C, 3 C, 5 C, 8 C, and 10 C (Figure 4c). The capacity of cells with an S@CoSA-N_3PS cathode at different current densities was 1057, 998, 936, 901, 873, 823, 709, and 619 mAh g^{-1}, respectively. In comparison, cells with S@CoSA-N_4 cathode and S@NPS cathode provided only a capacity of 452 and 311 mAh g^{-1} at 10 C, significantly lower than that of S@CoSA-N_3PS. These results suggest that P, S co-coordination regulating Co single atom is able to improve the catalytic activity of Co single atoms, thereby improving the redox kinetics of polysulfides. Moreover, the discharge voltage plateau at different rates from 0.2 C to 10 C is presented in Figure S34a–c (Supporting Information). The CoSA-N_3PS samples still display two obvious discharge plateaus even at high current densities, while the plateaus of CoSA-N_4 and NPS samples are inconspicuous at high rates. In addition, the cycle performance at low current density of the Li–S cells with S@CoSA-N_3PS, S@Co-N_4, and S@NPS cathodes is analyzed at 0.5 C in Figure 4d. The batteries with S@CoSA-N_3PS cathode showed a high initial capacity of 1098 mAh g^{-1} and retained 949 mAh g^{-1} after 200 cycles, thereby displaying a remarkable capacity retention rate of 86.4%. In comparison, the batteries with S@CoSA-N_4 and S@NPS cathodes only provided initial capacities of 1062 and 963 mAh g^{-1} and poor capacity retention of 36.7% and 34.8%. These results suggest P, S co-coordination regulates the d-orbital structure of single Co atoms, which are able to greatly enhance the activity of Co central atoms, confine polysulfides to the cathode, and catalyze the conversion of polysulfides in the case of low current density with a severe shuttle effect. As shown in Figure 4e, the batteries also show good cycling stability with a low capacity fading rate of 0.038% per cycle after 1000 cycles. The other two samples show a high-capacity fading rate of 0.061% and 0.074%, respectively, resulting from the severe polysulfides shuttle and sluggish redox conversion. Furthermore, even at a high current density of 3 C and 5 C, the batteries still exhibit impressive cycle stability with a high initial capacity of 881 and 812 mAh g^{-1} with a low fading rate of 0.063% per cycle after 500 cycles and 0.027% per cycle after 2000 cycles (Figure 4g; Figure S35, Supporting Information). More impressively, cycling 2000 cycles at the density of 5 C is the longest cycle at ultrahigh current density, which demonstrates excellent cycle stability with S@CoSA-N_3PS cathode. These outcomes demonstrate that Co single-atom catalysts coordinated with phosphorus and sulfur can effectively enhance the cycling stability and rate performance of Li–S batteries. To verify the practical applications for Li–S batteries using the S@CoSA-N_3PS cathode, the high sulfur loading performance was investigated because the shuttle effect is severe when the sulfur loading is higher. In this study, we tested the high sulfur loading performance with 2.2, 3.8, and 6 mg cm^{-2} at 0.2 C in Figure 4f. The batteries delivered an initial areal capacity of 2.4, 3, and 4.4 mAh cm^{-2}, with a capacity retention rate of 82%, 74%, and 75% after 60 cycles. In order to verify the practical application of the S@CoSA-N_3PS cathodes, cycle performance test at 1 C was also conducted with high mass loading of S of 3.2, 4.5, and 6.3 mg cm^{-2}, which achieves 200 cycles and delivers a high capacity of 2.1, 2.3, and 2.9 mAh cm^{-2}, respectively (Figure S36, Supporting Information). These outcomes prove the S@CoSA-N_3PS cathodes are able to restrict the shuttle effect and improve the redox kinetics of polysulfides conversion even at high sulfur loadings. Additionally, this work is also compared with other single-atom catalytic works to demonstrate its excellent structure and performance (Table S4, Supporting Information). It can be observed that this work not only achieves ultra-high rate cycling but also has significant advantages in high rate capacity, the number of cycles, and cycling stability.

In order to further characterize the influence of heteroatom coordination structures on electrochemical performance, CV tests were also conducted on CoSA-N_2PS_2 and CoSA-NPS_3 (Figure S37a, Supporting Information). The batteries with CoSA-N_2PS_2 and CoSA-NPS_3 also show two reduction peaks and one oxidation peak, which is ascribed to the reduction from S_8 to soluble Li_2S_n ($4 \leq n \leq 8$) and then to insoluble Li_2S or Li_2S_2, and the dissolution of Li_2S or Li_2S_2 to Li_2S_n, respectively. In addition, the results of tafel slope calculated from the CV curves can be found that the Tafel slope of S@CoSA-N_3PS is lower than that of S@CoSA-N_2PS_2 and CoSA-NPS_3, which demonstrates that the catalytic activity is also related to the number of coordinating heteroatoms and the relatively low catalytic activity may be ascribed to the introduction of more electrons by more heteroatoms, affecting the adsorption–desorption of polysulfides by the active center (Figure S37b,c, Supporting Information). The rate performance was also tested from 0.2 C to 10 C with S@CoSA-N_2PS_2 and S@CoSA-NPS_3 cathodes and the cells with S@CoSA-N_3PS cathode exhibited better rate performance compared with the other systems (Figure S38, Supporting Information). Moreover, the cycle performance at 0.5 C was also conducted, indicating that the batteries with S@CoSA-N_3PS are more stable than that with S@CoSA-N_2PS_2 and S@CoSA-NPS_3 (Figure S39, Supporting Information). This result may be due to the destruction of the dodecahedron morphology by high temperatures above 1000 °C, weakening the confinement effect on polysulfides. More impressively, the cycle performance of cells with S@CoSA-N_3PS, S@CoSA-N_2PS_2, and S@CoSA-NPS_3 at 2 C shows a high initial capacity of 925, 684, and 680 mAh g^{-1} with capacity retention of 81.6%, 76.4%, and 61.4%, respectively (Figure S40, Supporting Information).

In situ Raman spectroscopy was conducted to delve into the mechanism of polysulfides conversion during the charge/discharge process. For batteries with an S@NPS cathode, **Figure 5a** reveals evident signals of long-chain and medium-chain polysulfides. The peaks of long-chain polysulfides appear at 195, 393, 448, and 504 cm^{-1} at the beginning of discharge, which correspond to S_6^{2-} and S_8^{2-} species, respectively. The characteristic peaks of S_5^{2-} and S_4^{2-} strengthen at the second discharge plateau and persist until the end. Planar and 3D in situ time-resolved Raman spectra in Figure 5b,c provide a more intuitive observation of peak changes during the discharge process, indicating a severe shuttle effect when utilizing the S@NPS cathode. In contrast, batteries with an S@CoSA-N_3PS cathode show almost no characteristic peaks of polysulfides during the discharge process (Figure 5d-f). This suggests that polysulfides are effectively confined to the cathode side, alleviating the shuttle effect of polysulfides due to the outstanding adsorptive and catalytic performance of the unique CoSA-N_3PS moiety. Time-of-flight secondary ion mass spectrometry (ToF-SIMS) further proved the confinement and catalytic effect of CoSA-N_3PS on polysulfides. Figure 5g,h shows weaker intensities of secondary S^- ions at the surface of S@CoSA-N_3PS cathodes after 100 cycles at 1 C compared to S@NPS, indicating less sulfur agglomeration on the S@CoSA-N_3PS cathode surface. Additionally, TOF-SIMS 3D images in Figure 5j,k illustrate that S^- is more concentrated on the surface of the S@NPS electrode, while S^- is mostly inside the cycled S@CoSA-N_3PS cathode and increases with sputtering time, in accordance with the ToF-SIMS depth profiles in Figure 5i. These outcomes demonstrate that sulfur species are more effectively confined within the nanocages of CoSA-N_3PS, promoting redox reactions of polysulfides and preventing the accumulation of dead sulfur species on the material's surface,

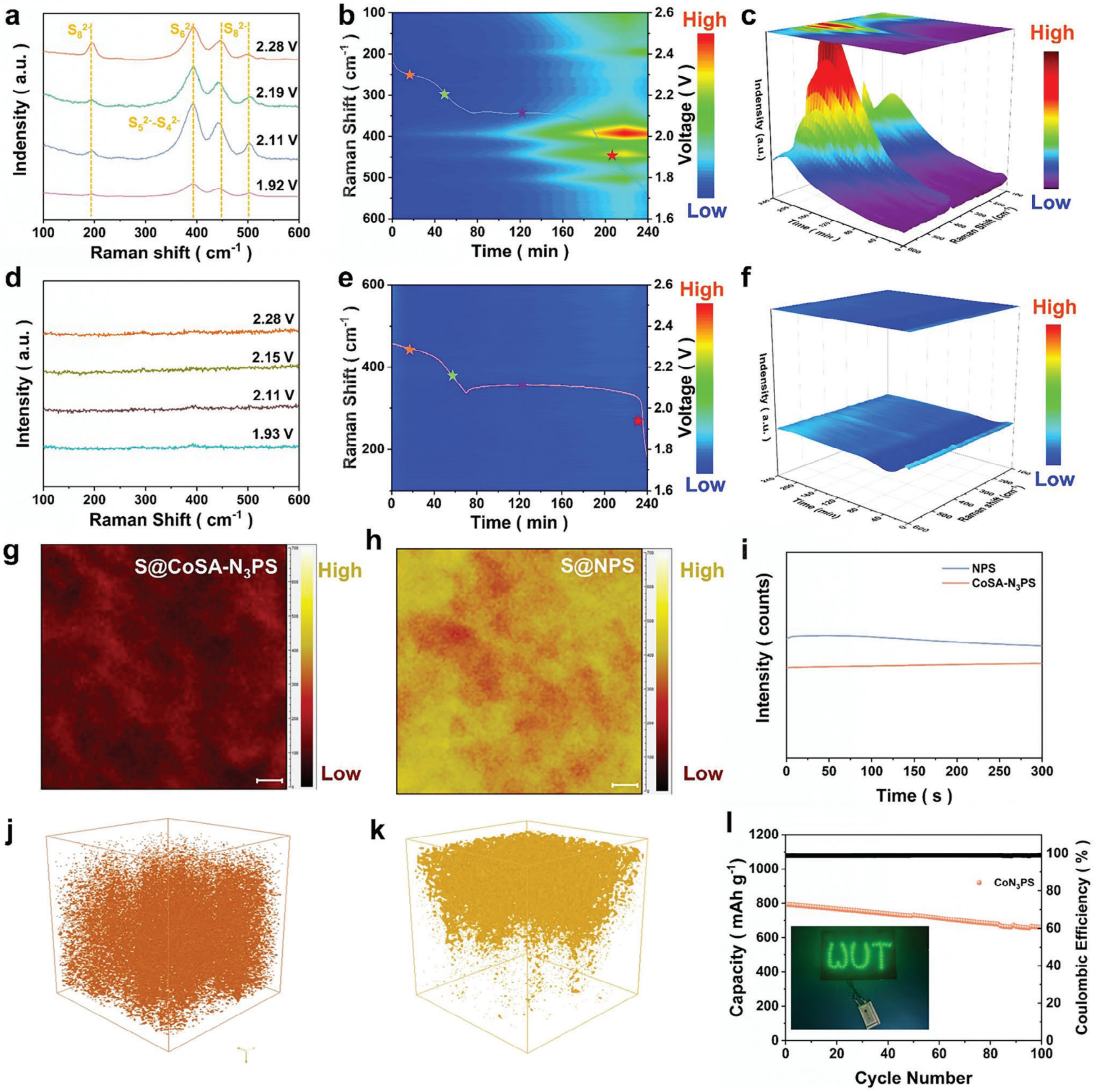

Figure 5. a,d) In situ Raman spectrum of S@CoSA-N$_3$PS and S@NPS. b,c,e,f) The corresponding planar and 2D and 3D in situ time-resolved Raman spectra (g,h) ToF-SIMS S$^-$ element mappings on the top surface. i) ToF-SIMS 3D rendering S$^-$ depth profile image. j,k) ToF-SIMS 3D rendering S$^-$ depth profile image. l) Cycle performance of a pouch battery with S@CoSA-N$_3$PS at 0.2 C. Inset: Photos of pouch Li–S battery with S@CoSA-N$_3$PS cathode light the "WUT" logo.

which could otherwise impede electron and ion conduction. For a comprehensive evaluation of the potential application of the S@CoSA-N$_3$PS cathode, Li–S pouch cells were assembled, still providing a high initial capacity of 660 mAh g−^{1} after 100 cycles. Moreover, the battery illuminated the LED light with the "WUT" logo for an extended period, implying the potential applications of S@CoSA-N$_3$PS in the state-of-the-art Li–S batteries (Figure 5l).

To elucidate the regulatory mechanism of phosphorus-sulfur heteroatom coordination on single atoms and the impact of high coordination Co single atoms on polysulfides, Density functional theory (DFT) calculations were employed to study the atomic-level structure. In Figure S41a–c (Supporting Information), the optimized substrate configurations of CoSA-N$_3$PS, CoSA-N$_4$, and NPS are displayed for studying adsorption conformations. The Density of States (DOS) of CoSA-N$_3$PS, CoSA-N$_4$, and NPS

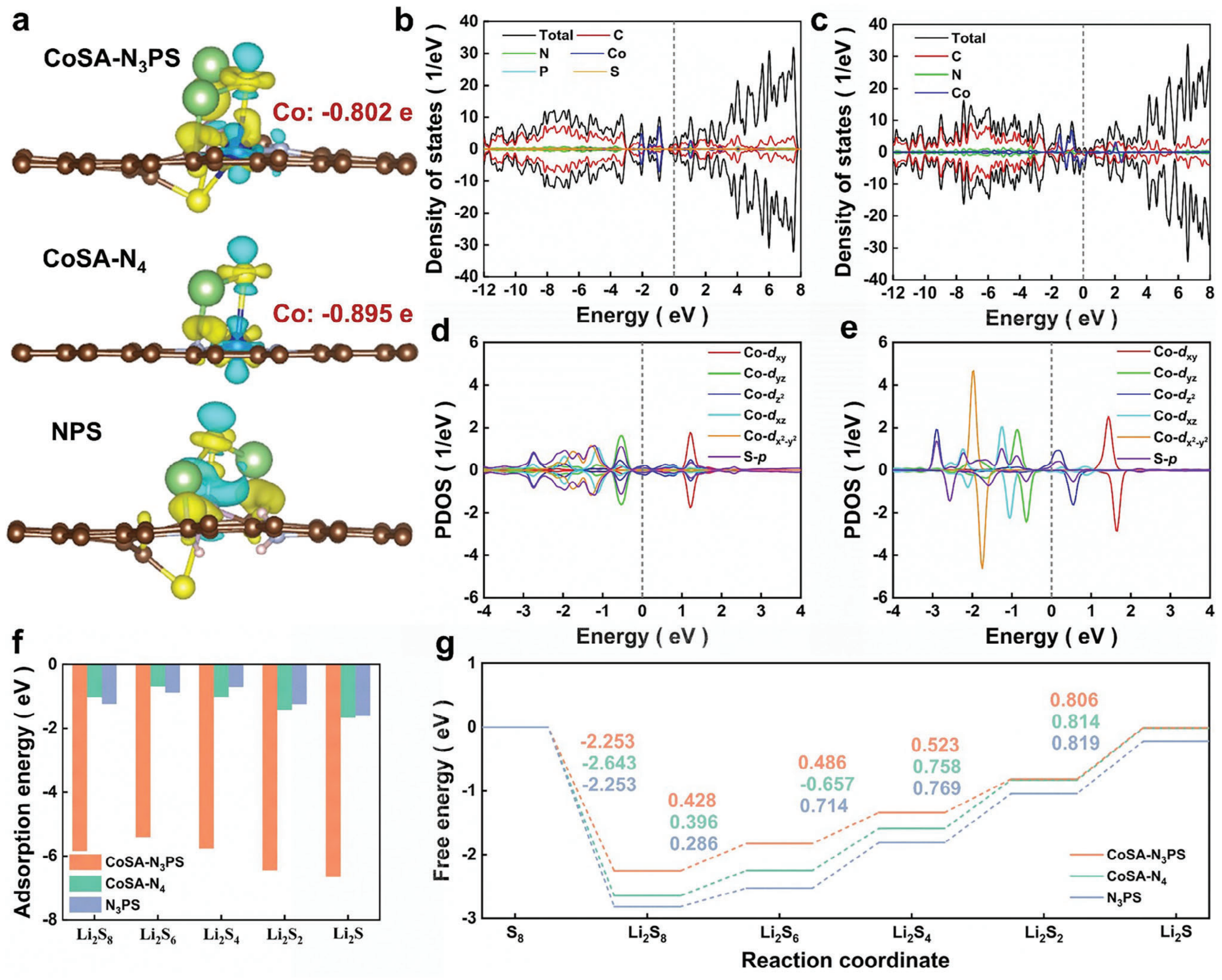

Figure 6. a) Simulated deformation charge density of CoSA-N$_3$PS, CoSA-N$_4$, and NPS (b-c) DOS of CoSA-N$_3$PS and CoSA-N$_4$ systems. d,e) PDOS of Co-d orbitals and S-p orbitals of Li$_2$S for d) CoSA-N$_3$PS and e) CoSA-N$_4$. f) Calculated adsorption energy of various polysulfides adsorbed on different catalysts. g) Gibbs free energy of sulfur reduction process on CoSA-N$_3$PS, CoSA-N$_4$, and NPS.

suggests valence bands crossing the Fermi level, facilitating electron transfer during polysulfide conversion (**Figure 6**b,c; Figure S42, Supporting Information). To further investigate the d-p orbital hybridization between Co atoms and S atoms of polysulfides, the DOS of Li$_2$S on different substrates was calculated (Figures S43 and S44a–c, Supporting Information). The valence bands of multiple atoms pass through the Fermi level, indicating good reaction activity of substrates with Li$_2$S. In Figure 6d,e, PDOS of Co-d orbitals and S-p orbitals of Li$_2$S with a CoSA-N$_3$PS substrate exhibit stronger d-p orbital hybridization at the Fermi level than that of CoSA-N$_4$, and there is no hybridization of Co and S in the DOS of CoSA-N$_3$PS. This confirms that P, S co-coordination regulates the electron structure of the Co central atom, strengthening d-p orbital hybridization between Co and S. Furthermore, simulated deformation charge density shows different catalysts undergo charge transfer during interaction with Li$_2$S (Figure 6a; Figure S45a–c, Supporting Information). Bader charge analysis, calculated from simulated deformation charge density, reveals that Co in CoSA-N$_3$PS delivers a Bader charge of −0.802 e, lower than that of Co in CoSA-N$_4$ (−0.895 e). This indicates that the P, S co-coordination structure helps retain more 3d orbital electrons of Co atoms, facilitating polysulfide adsorption and accelerating the polysulfides conversion. Figure S46a–f (Supporting Information) presents the optimized adsorption configurations for different polysulfides on the CoSA-N$_3$PS substrate, demonstrating Lewis acid–base interaction of Co and S, as well as electrostatic adsorption of Li and N. In Figure 6f, due to the regulatory effect of P, S co-coordination on the d orbital electrons of Co single atoms, it presents stronger d-p orbital hybridization with S atoms in polysulfides, resulting in stronger adsorption energies of CoSA-N$_3$PS for polysulfides, with values higher than CoSA-N$_4$ and NPS (Figure S47a–f and S48a–f, Supporting Information). These results align with the visualized adsorption test. Additionally, Gibbs free energy (ΔG) was calculated for the sulfur reduction process to analyze the thermodynamic transformation tendency of polysulfides. In Figure 6g, the Gibbs free energy of CoSA-N_3PS is significantly lower than the other two samples for the rate-limiting step Li_2S_4-Li_2S, indicating CoSA-N_3PS improves the reaction kinetics of polysulfides. Moreover, Li_2S decomposition is a sluggish reaction during the oxidation process, impacting the overall redox kinetics. Benefiting from the high catalytic activity of CoSA-N_3PS, the reaction energy barrier of the CoSA-N_3PS surface is lower than that of CoSA-N_4, confirming the configuration of CoSA-N_3PS accelerates the solid–liquid conversion of polysulfides (Figure S49a,b, Supporting Information). These theoretical calculations demonstrate that P, S co-coordination regulation effectively enhances the catalytic activity of central cobalt single atoms, facilitating the adsorption and catalysis of polysulfides, and promoting bidirectional redox kinetics.

3. Conclusion

In summary, we have successfully synthesized a novel asymmetric configuration of CoSA-N_3PS single-atom catalyst, featuring coordinated phosphorus and sulfur (P, S co-coordination), using a two-step pyrolysis method to enhance the activity of the central cobalt atom. The high-coordination structure of CoSA-N_3PS was confirmed through high-angle annular dark-field scanning transmission electron microscopy (HAADF-STEM), X-ray absorption near-edge structure (XANES), and Fourier-transformed extended X-ray absorption fine structure (FT-EXAFS) spectra. More impressively, the density of states calculations revealed that the optimized Co 3d electrons strengthen d-p orbital hybridization between Co single atoms and S atoms in polysulfides and the simulated deformation charge density demonstrates the P, S co-coordination retains more 3d orbital electrons of Co atoms. These advantages enable the Co center to exhibit remarkable adsorptive and catalytic activity, which are proved by electrocatalytic tests and Gibbs free energy calculation, leading to outstanding performance in advanced Li–S batteries. The cells with S@CoSA-N_3PS cathode demonstrated ultralong cycle life and excellent rate performance, with an ultra-low-capacity fading rate of 0.038% after 1000 cycles at 1 C and 0.027% after 2000 cycles at a high rate of 5 C. Moreover, the batteries achieved an ultrahigh capacity of 619 mAh g^{-1} at an ultrahigh current density of 10 C. Impressively, even with a high sulfur loading of 6 mg cm^{-2}, the batteries maintained a capacity of 4.4 mAh cm^{-2} and validate practical applications when assembling a Li–S pouch cell with an S@CoSA-N_3PS cathode. This work introduces a novel approach, incorporating P, S dual heteroatoms to regulate the coordination environment of single metal atoms in an asymmetric manner. It opens up opportunities for the rational design of catalysts in the development of the advanced Li–S batteries.

Supporting Information

Supporting Information is available from the Wiley Online Library or from the author.

Acknowledgements

C.X.D. and C.N.M. contributed equally to this work. This work was supported by the National Natural Science Foundation of China (No. U23A20555), the National Energy-Saving and Low-Carbon Materials Production and Application Demonstration Platform Program (TC220H06N), and the National Innovation and Entrepreneurship Training Program for College Students (No. S202310497015). The authors would like to acknowledge the Synchrotron Light Research Institute (Public Organization), SLRI, for the provision of beamtime, and the author appreciates Dr. Suttipong Wannapaiboon and the staffs of beamline 1.1 W for their assistance.

Conflict of Interest

The authors declare no conflict of interest.

Data Availability Statement

The data that support the findings of this study are available from the corresponding author upon reasonable request.

Keywords

coordination regulation, electrocatalysis, lithium–sulfur batteries, single atom catalyst

Received: May 18, 2024
Revised: July 10, 2024
Published online: August 1, 2024

---

[1] J.-M. Tarascon, M. Armand, *Nature* **2001**, *414*, 359.
[2] L. Wang, W. Hua, X. Wan, Z. Feng, Z. Hu, H. Li, J. Niu, L. Wang, A. Wang, J. Liu, X. Lang, G. Wang, W. Li, Q. H. Yang, W. Wang, *Adv. Mater.* **2022**, *34*, 2110279.
[3] G. Zhou, H. Chen, Y. Cui, *Nat. Energy* **2022**, *7*, 312.
[4] C. Zhou, C. Dong, W. Wang, Y. Tian, C. Shen, K. Yan, L. Mai, X. Xu, *Interdiscip. Mater.* **2024**, *3*, 306.
[5] C. Dong, C. Zhou, M. Wu, Y. Yu, K. Yu, K. Yan, C. Shen, J. Gu, M. Yan, C. Sun, L. Mai, X. Xu, *Adv. Energy Mater.* **2023**, *13*, 2301505.
[6] W. Yao, C. Tian, C. Yang, J. Xu, Y. Meng, I. Manke, N. Chen, Z. Wu, L. Zhan, Y. Wang, R. Chen, *Adv. Mater.* **2022**, *34*, 2106370.
[7] Y. Li, S. Guo, *Matter.* **2021**, *4*, 1142.
[8] S. Zhang, X. Ao, J. Huang, B. Wei, Y. Zhai, D. Zhai, W. Deng, C. Su, D. Wang, Y. Li, *Nano Lett.* **2021**, *21*, 9691.
[9] R. Wang, R. Wu, X. Yan, D. Liu, P. Guo, W. Li, H. Pan, *Adv. Funct. Mater.* **2022**, *32*, 2200424.
[10] R. Bai, Q. Lin, X. Li, F. Ling, H. Wang, S. Tan, L. Hu, M. Ma, X. Wu, Y. Shao, X. Rui, E. Hu, Y. Yao, Y. Yu, *Angew. Chem., Int. Ed.* **2023**, *62*, 202218165.
[11] H. Wang, Y. Yang, Y. Liang, J. T. Robinson, Y. Li, A. Jackson, Y. Cui, H. Dai, *Nano Lett.* **2011**, *11*, 2644.
[12] C. Hu, H. Chen, Y. Shen, D. Lu, Y. Zhao, A.-H. Lu, X. Wu, W. Lu, L. Chen, *Nat. Commun.* **2017**, *8*, 479.
[13] C. Zhou, M. Chen, C. Dong, H. Wang, C. Shen, X. Wu, Q. An, G. Chang, X. Xu, L. Mai, *Nano Energy* **2022**, *98*, 107332.
[14] M. Fang, J. Han, S. He, J.-C. Ren, S. Li, W. Liu, *J. Am. Chem. Soc.* **2023**, *145*, 12601.
[15] B. Wang, L. Wang, B. Zhang, S. Zeng, F. Tian, J. Dou, Y. Qian, L. Xu, *ACS Nano* **2022**, *16*, 4947.
[16] B. Fei, C. Zhang, D. Cai, J. Zheng, Q. Chen, Y. Xie, L. Zhu, A. Cabot, H. Zhan, *ACS Nano* **2021**, *15*, 6849.
[17] Y. Wang, J. Mao, X. Meng, L. Yu, D. Deng, X. Bao, *Chem. Rev.* **2019**, *119*, 1806.

[18] G. Zhang, Y. Jia, C. Zhang, X. Xiong, K. Sun, R. Chen, W. Chen, Y. Kuang, L. Zheng, H. Tang, W. Liu, J. Liu, X. Sun, W.-F. Lin, H. Dai, *Energy Environ. Sci.* **2019**, *12*, 1317.

[19] Y. Chen, R. Gao, S. Ji, H. Li, K. Tang, P. Jiang, H. Hu, Z. Zhang, H. Hao, Q. Qu, X. Liang, W. Chen, J. Dong, D. Wang, Y. Li, *Angew. Chem., Int. Ed.* **2021**, *60*, 3212.

[20] C. Dong, C. Zhou, Y. Li, Y. Yu, T. Zhao, G. Zhang, X. Chen, K. Yan, L. Mai, X. Xu, *Small* **2023**, *19*, 2205855.

[21] Z. Shen, X. Jin, J. Tian, M. Li, Y. Yuan, S. Zhang, S. Fang, X. Fan, W. Xu, H. Lu, J. Lu, H. Zhang, *Nat. Catal.* **2022**, *5*, 555.

[22] P. Wang, B. Xi, Z. Zhang, M. Huang, J. Feng, S. Xiong, *Angew. Chem., Int. Ed. Engl.* **2021**, *60*, 15563.

[23] Y. Li, G. Chen, J. Mou, Y. Liu, S. Xue, T. Tan, W. Zhong, Q. Deng, T. Li, J. Hu, C. Yang, K. Huang, M. Liu, *Energy Storage Mater.* **2020**, *28*, 196.

[24] X. Zhang, T. Yang, Y. Zhang, X. Wang, J. Wang, Y. Li, A. Yu, X. Wang, Z. Chen, *Adv. Mater.* **2023**, *35*, 2208470.

[25] L. Ren, K. Sun, Y. Wang, A. Kumar, J. Liu, X. Lu, Y. Zhao, Q. Zhu, W. Liu, H. Xu, X. Sun, *Adv. Mater.* **2023**, *36*, 2310547.

[26] T. Sun, S. Mitchell, J. Li, P. Lyu, X. Wu, J. Pérez-Ramírez, J. Lu, *Adv. Mater.* **2021**, *33*, 2003075.

[27] J. Kim, S.-J. Kim, E. Jung, D. H. Mok, V. K. Paidi, J. Lee, H. S. Lee, Y. Jeoun, W. Ko, H. Shin, B.-H. Lee, S.-Y. Kim, H. Kim, J. H. Kim, S.-P. Cho, K.-S. Lee, S. Back, S.-H. Yu, Y.-E. Sung, T. Hyeon, *Adv. Funct. Mater.* **2022**, *32*, 2110857.

[28] L. Yin, S. Zhang, M. Sun, S. Wang, B. Huang, Y. Du, *Adv. Mater.* **2023**, *35*, 2302485.

[29] W. Guo, Z. Wang, X. Wang, Y. Wu, *Adv. Mater.* **2021**, *33*, 2004287.

[30] X. Li, H. Rong, J. Zhang, D. Wang, Y. Li, *Nano Res.* **2020**, *13*, 1842.

[31] Z. Du, X. Chen, W. Hu, C. Chuang, S. Xie, A. Hu, W. Yan, X. Kong, X. Wu, H. Ji, L.-J. Wan, *J. Am. Chem. Soc.* **2019**, *141*, 3977.

[32] D. Guo, X. Zhang, M. Liu, Z. Yu, X. Chen, B. Yang, Z. Zhou, S. Wang, *Adv. Funct. Mater.* **2022**, *32*, 2204458.

[33] Z. Han, S. Zhao, J. Xiao, X. Zhong, J. Sheng, W. Lv, Q. Zhang, G. Zhou, H. Cheng, *Adv. Mater.* **2021**, *33*, 2105947.

[34] H. Gu, W. Yue, J. Hu, X. Niu, H. Tang, F. Qin, Y. Li, Q. Yan, X. Liu, W. Xu, Z. Sun, Q. Liu, W. Yan, L. Zheng, Y. Wang, H. Wang, X. Li, L. Zhang, G. Xia, W. Chen, *Adv. Energy Mater.* **2023**, *13*, 2204014.

[35] S. Li, J. Lin, B. Chang, D. Yang, D.-Y. Wu, J. Wang, W. Zhou, H. Liu, S. Sun, L. Zhang, *Energy Storage Mater.* **2023**, *55*, 94.

[36] W. Lim, C. Park, H. Jung, S. Kim, S. H. Kang, Y. Lee, Y. C. Jeong, S. B. Yang, K. Sohn, J. W. Han, J. Lee, *Adv. Mater.* **2023**, *35*, 2208999.

[37] T. Sun, F. Huang, J. Liu, H. Yu, X. Feng, X. Feng, Y. Yang, H. Shu, F. Zhang, *Adv. Funct. Mater.* **2023**, *33*, 2306049.

[38] Y. Zhang, J. Liu, J. Wang, Y. Zhao, D. Luo, A. Yu, X. Wang, Z. Chen, *Angew. Chem., Int. Ed.* **2021**, *60*, 26622.

[39] T. Huang, Y. Sun, J. Wu, Z. Shi, Y. Ding, M. Wang, C. Su, Y. Li, J. Sun, *Adv. Funct. Mater.* **2022**, *32*, 2203902.